Medium-pressure hydrogen storage on activated carbon derived from biomass conversion

Fuel 363 (2024) 130975

Contents lists available at ScienceDirect

Fuel

journal homepage: www.elsevier.com/locate/fuel

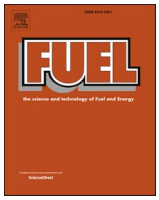

Full Length Article

Medium-pressure hydrogen storage on activated carbon derived from biomass conversion

Jarosław Serafin [a,b,*], Bartosz Dziejarski [a,c,d], Carlos Solis [a], Pilar Ramírez de la Piscina [a,e], Narcis Homs [a,e,f]

[a] Department of Inorganic and Organic Chemistry, Inorganic Chemistry section, University of Barcelona, Martí i Franquès 1-11, 08028 Barcelona, Spain
[b] ENPHOCAMAT (FEMAN) Group, Department of Applied Physics, Universitat de Barcelona, Martí i Franquès 1, E-08028 Barcelona, Spain
[c] Faculty of Environmental Engineering, Wroclaw University of Science and Technology, 50-370 Wroclaw, Poland
[d] Department of Space, Earth and Environment, Division of Energy Technology, Chalmers University of Technology, SE-412 96 Gothenburg, Sweden
[e] Institute of Nanoscience and Nanotechnology (IN2UB), University of Barcelona, Spain
[f] Catalonia Institute for Energy Research (IREC), Jardins de les Dones de Negre 1, 08930 Barcelona, Spain

ARTICLE INFO

Keywords:
Biomass-based activated carbon
Hydrogen storage
KOH activation
Net-zero emission
Adsorption mechanism

ABSTRACT

This study presents the utilization of activated carbons (ACs) derived from Polypodium vulgare, a commonly available feedstock, for effective medium-pressure H_2 storage. For the ACs preparation, biomass was treated with KOH and then pyrolyzed at 700–900 °C. H_2 adsorption was performed at 25–100 °C and pressures up to 45 bar; nine different models (Langmuir, Freundlich, Temkin, Redlich–Peterson, Toth, Hill, Koble–Corrigan, Sips, and Radke–Prausnitz) were used for adjusting experimental H_2 adsorption isotherms. The micropore volume in the ranges 1.4–2 nm and 0.3–1.4 nm was determined by N_2 and CO_2 adsorption at −196 and 0 °C, respectively. The textural characteristics and the H_2 storage capacity of ACs depended on the carbonization temperature. All samples exhibited a considerable specific surface area of 1234–1591 m^2/g, and significant volume of micropores with size below 1.4 nm. The H_2 adsorption capacity is related with the micropore volume determined by CO_2 adsorption. The AC prepared at 800 °C (G-800) showed the highest H_2 uptake and both the highest specific surface area and volume of micropores with size below 1.4 nm. G-800 adsorbs 13.63 mmol H_2/g (2.73 wt%) at 25 °C and 45 bar. G-800 sample also showed exceptional cyclic stability, keeping its adsorption capabilities after undergoing multiple adsorption–desorption cycles. The isosteric heat of adsorption of ACs was determined using the Clausius-Clapeyron equation, yielding values ranging from 5.7 to 7.7 kJ/mol.

1. Introduction

In recent years, the future need for a hydrogen-based economy has been recognized. In the past, hydrogen was primarily generated through processes like steam methane reforming (SMR) and coal gasification, which relied heavily on fossil fuels, resulting in greenhouse gas emissions. Today, there is a growing emphasis on cleaner production methods, particularly electrolysis powered by renewable energy sources. Its main advantage is that only water and heat are generated during its utilization, while not emitting CO_2, thus reducing greenhouse gas emissions, and mitigating air pollution. In addition, H_2O can be used to regenerate hydrogen by direct electrolysis using renewable energy, resulting in a closed cycle [1–3]. This shift is driven by the need to reduce the current global average concentration of CO_2 in the atmosphere and address environmental concerns. In view of this, the benefits of using renewable hydrogen are both strategic and environmental [4,5]. Furthermore, progress in the development of hydrogen storage and transportation technologies has facilitated the incorporation of hydrogen into different sectors, including transportation, industry, and energy, as an environmentally friendly energy carrier. This has the potential to significantly to play a significant role towards a low-carbon economy [6]. Consequently, one of the major challenges in using hydrogen as energy vector is its storage in a safe and efficient manner [7]. H_2 has high energy content, but low energy density under standard conditions [8], it also possesses high reactivity, and it is difficult to handle. Therefore, developing cost-effective and efficient methods of

* Corresponding author at: Department of Inorganic and Organic Chemistry, Inorganic Chemistry section, University of Barcelona, Martí i Franquès 1-11, 08028 Barcelona, Spain.
E-mail address: jaroslaw.serafin@qi.ub.es (J. Serafin).

https://doi.org/10.1016/j.fuel.2024.130975
Received 8 November 2023; Received in revised form 15 December 2023; Accepted 11 January 2024
Available online 18 January 2024

storage is essential for its widespread adoption on a commercial scale in the energy sector.

There are several approaches to H_2 storage, including compressed gas at high pressure, the use of cryogenic liquids in specialized tanks and the formation of hydrides [9–11]. Each of these methods has its own advantages and disadvantages, and the most suitable approach depends on the specific application. Carriers of hydrogen, such as ammonia (NH_3), and solid materials play crucial roles on this field [12–14]. Recently, one storage strategy for H_2 that has garnered considerable attention is the utilization of the adsorption phenomenon [15,16]. For this aim the understanding of the interactions between H_2 and the solid surface is crucial. A wide variety of different types of solid sorbents can be applied for hydrogen storage, including metal–organic frameworks (MOFs), zeolites, and carbon-based materials [17–19]. Among them, activated carbon with low production cost, high surface area and high affinity towards H_2, is an attractive option. These materials should meet several requirements for a reasonable working volume, weight, effective kinetics of charging and discharging, safe operation, stability under different conditions, low cost, and technological simplicity. Adsorbents having a high affinity for hydrogen enable them to store a large amount in a small volume. They can be applied for storage at room temperature and atmospheric pressure, which makes them a potentially safe and convenient option [20]. The exploration of sustainable and efficient hydrogen storage materials has become crucial for the development of clean energy technologies.

In general, adsorbents with high surface area, well-developed pore size distribution and structure, high affinity toward hydrogen, and hydrogen storage systems working at mild temperature and pressure, are preferred [21]. In order to maximize the hydrogen storage capacity of a solid sorbent, it is necessary to optimize these properties and to design the adsorbent with a suitable microstructure and chemical composition.

In this study, the primary objective of this research is to comprehensively investigate the medium-pressure adsorption behavior of hydrogen on activated carbons (ACs) derived from common fern leaves (polypodium vulgare), an abundant and rapidly growing residual biomass. ACs were prepared by a controlled pyrolysis process, resulting in porous structures with a high specific surface area. Our focus on medium-pressure hydrogen adsorption isotherms aims to unravel the unique adsorption characteristics of biomass-derived ACs. Moreover, the environmentally friendly nature of biomass feedstock underscores the attractiveness of derived ACs as sustainable candidates for energy storage systems. The results demonstrate that the ACs prepared exhibit performant hydrogen adsorption capacity at medium pressures. The findings of this study contribute to the understanding of biomass-derived ACs as potential materials for medium-pressure hydrogen storage. Furthermore, the environmentally friendly nature of biomass feedstock makes derived ACs attractive candidates for a greener and more sustainable future in energy storage technologies.

2. Research methodology

2.1. Preparation of activated carbon from biomass

The leaves of Polypodium vulgare were dried at 105 °C for 24 h and then finely pulverized (Table 1). The powder was blended with a saturated KOH solution (KOH/powder biomass = 1/1 wt/wt) and kept at ambient temperature for 3 h. Afterwards, the mixture was dried at 200° C for 18 h, and then carbonized for 1 h under N_2 flow (15 dm^3/h) within the interval of 700–900 °C. Samples were subsequently washed with distilled water until pH = 7 and treated with a 1 M HCl for 18 h. After that, the complete removal of chloride ions with distilled water was carried out. Finally, the obtained materials were treated at 200 °C in an oven for 16 h. The activated carbons were named G-XXX, where XXX corresponds to the carbonization temperature. Thus, for example, G-900 means a sample carbonized at 900 °C.

Table 1
Elemental analysis of activated carbons precursor.

Sample	Elemental analysis			
	C [wt%]	H [%]	N[%]	O[%]
Fern leaves	78.89	6.45	2.83	11.83

2.2. Materials characterization

To analyze the textural properties of the ACs samples, nitrogen adsorption/desorption isotherms at −196 °C and CO_2 adsorption measurements at 0 °C were conducted using a QUADRASORB evo™ apparatus. The specific surface area of the developed ACs was estimated using the Brunauer-Emmett-Teller (BET) equation, based on the adsorption data at relative pressures (P/P^0) ranging from 0.05 to 0.25. The total pore volume (V_{tot}) at the maximum relative pressure (P/P^0 = 0.99) was determined from the N_2 adsorption isotherms. The porosity of the AC samples, including pore size and pore size distributions, was determined using the non-local density functional theory model, which utilized experimental data from N_2 and CO_2 adsorption isotherms at −196 °C and 0 °C, respectively. The study of microporosity with pore sizes ranging from 0.30 to 1.47 nm was enabled by the adsorption of CO_2 at 0 °C. The sorption analyzer, QUADRASORB evo™ was also utilized to assess the H_2 capture performance of ACs at ambient pressure. Measurements of H_2 adsorption were executed with high-purity H_2 (99.999 %) at 25, 40, 60, 80, and 100 °C, up to 45 bar. Before the adsorption experiments, the ACs underwent a meticulous degassing procedure lasting 16 h under vacuum at 200 °C. The stability of ACs as adsorbents was tested in 1, 3, 5, and 10 cycles at 25 °C, 40 °C, 60 °C, 80 °C, and 100 °C up to 45 bar. Each cycle included full adsorption and then desorption.

XRD analysis of ACs was achieved by employing a PANalytical Empyrean diffractometer, which harnessed the illuminating power of Cu Kα radiation (λ = 0.154 nm). The 2θ analyzed was 20-100°.

The FTIR spectra of all the samples were acquired using a Thermo Scientific Nicolet 6700 FTIR spectrometer, which was equipped with a CsI beam splitter. The spectral data were recorded over the range 500–4000 cm^{-1}.

Raman spectra were acquired using an InVia Raman Microscope spectrometer, which was equipped with a 785 nm laser. Subsequent to the preliminary step of standardizing the intensity of the G peak to 1 in each spectrum, the discernment and determination of D peaks' intensity and location were undertaken.

Examination of ACs by scanning electron microscopy (SEM) was conducted utilizing the Ultra-high Resolution Scanning Electron Microscope Hitachi SU8000, which was outfitted with an EDS X-ray microanalyzer and cold emission source (HITACHI UHR FE-SEM). Additionally, transmission electron microscopy (TEM) was performed using a JEOL NEOARM 200F operating at 30–200 Kv.

2.3. Fitting of adsorption isotherms

In this work, nine different isotherm models were employed to fit the H_2 experimental data, such as: two-parameter (Langmuir, Freundlich, Temkin), and three-parameter (Redlich–Peterson, Toth, Hill, Koble–Corrigan, Sips, Radke–Prausnitz). According to the isotherm assumptions, the description of the adsorption phenomenon and the equation of the different models are shown in Table 2.

To appropriately modeling the selected isotherm equations to empirical adsorption equilibrium measurements, non-linear regression analysis were performed using the Solver Add-In in Microsoft Excel. This allowed for a specific isotherm equation, the determination of the parameter values that best fit the data. To evaluate the quality of fitting in isotherm modeling, we have estimated the sum of squares error (SSE); a lower SSE value indicates a better fit. The SSE is calculated by sum-

Table 2
Description of selected adsorption isotherm models.

Isotherm model	Described adsorption phenomenon	Non-linear model equations	Parameters of the equation	Ref.
Langmuir	Monolayer adsorption on homogeneous surface	$q_e = q_m \frac{K_L \bullet P}{(1 + K_L \bullet P)}$	q_e - experimental amount of adsorbed adsorbate [mmol/g], q_m - maximum adsorption capacity (mmol/g), P - relative pressure of the adsorbate (bar), K_L - Langmuir isotherm constant (bar^{-1})	[57]
Freundlich	Multilayer adsorption on heterogeneous surface	$q_e = K_F \bullet p^{\frac{1}{n_F}}$	K_F - Freundlich isotherm constant (bar^{-1}), $1/n_F$ – heterogeneity factor, n_F – Freundlich exponent (–)	[58]
Redlich–Peterson	Includes the features of both Langmuir and Freundlich isotherm	$q_e = \frac{K_{RP} \bullet P}{1 + a_{RP} \cdot P^{\beta_{RP}}}$	K_{RP} - Redlich-Peterson isotherm constant (bar^{-1}), a_{RP} - Redlich-Peterson model constant (bar^{-1}), β_{RP} – exponent (–)	[59]
Toth	Adsorption on heterogeneous surfaces	$q_e = \frac{q_m \bullet K_T \bullet P}{[1 + (K_T \bullet P)^{n_T}]^{\frac{1}{n_T}}}$	q_m - maximum adsorption capacity (mmol/g), K_T - Toth isotherm constant (bar^{-1}), n_T – heterogeneity factor (–)	[60]
Hill	Binding capability during adsorption of the gas molecules onto homogeneous surface	$q_e = \frac{q_H \bullet P^{n_H}}{K_D + P^{n_H}}$	q_H - maximum uptake saturation (bar), P - relative pressure of the adsorbate (bar), K_H - Hill isotherm constant, n_H -Hill cooperativity coefficient of binding interaction (–)	[61]
Koble–Corrigan	Incorporation both Langmuir and Freundlich isotherm	$q_e = \frac{A \bullet P^{n_{KC}}}{1 + B \bullet P^{n_{KC}}}$	A - Koble-Corrigan isotherm constant (mmol/g), B - Koble-Corrigan isotherm constant (bar^{-1}), n_{KC} - Koble-Corrigan isotherm model exponent (–)	[62]
Sips	Combined form of the Langmuir and Freundlich model equations to characterize heterogeneous adsorption systems	$q_e = \frac{q_m \bullet (K_S \bullet P)^{\frac{1}{n_S}}}{1 + (K_S \bullet P)^{\frac{1}{n_S}}}$	q_m - maximum adsorption capacity (mmol/g), K_S - Sips isotherm constant (bar^{-1}), n_S – Sips isotherm exponent (–)	[63]
Radke–Prausnitz	Adsorption with low concentration of the gas molecules	$q_e = \frac{q_m \bullet K_{RPr} \bullet P}{1 + K_{RPr} \cdot P^{e_{RPr}}}$	q_m is maximum adsorption capacity (mmol/g), K_{RPr} is Redlich- Prausnitz isotherm constant (bar^{-1}), and e_{RPr} is the model exponent (–)	[64]
Temkin	Adsorption occurring on heterogeneous surfaces with a nonuniform energy distribution	$q_e = B \bullet \ln(K_T \bullet P)$	B -Temkin constant (–), K_T - adsorption equilibrium constant (bar^{-1})	[65]

ming the squares of the differences between the observed data points and the predicted values of the dependent variable based on the model. Specifically, the SSE is given by the following formula [22]:

$$SSE = \sum_{i=1}^{n} (q_{e,observed} - q_{e,predicted})^2 \quad (1)$$

where $q_{e,observed}$ are the experimental amounts of H_2 adsorbed at equilibrium [mmol/g] and $q_{e,predicted}$ the theoretical ones derived from a given isotherm model [mmol/g].

2.4. Thermodynamic studies

In this study, the isosteric heats of adsorption (Q_{st}) of H_2 onto the different ACs were determined. The Qst is a direct indicator of the strength of the adsorbate interaction with the adsorbent surface, it reflects the average binding energy of a gas molecule adsorbing at a certain surface coverage and is an essential thermodynamic parameter for the design and optimization of realistic gas separation technologies [23–25]. The Q_{st} values (kJ/mol) of H_2 were determined from adsorption isotherms at different temperatures, using the Clausius-Clapeyron equation:

$$\frac{Q_{st}}{R} = \left(\frac{\partial(\ln(p))}{\partial\left(\frac{1}{T}\right)} \right)_{q_e} \quad (2)$$

where p is the partial pressure of H_2 at equilibrium (Pa) T is the temperature (K), R is the ideal gas constant R = 8.314 J/mol/K) and q_e indicates the specific amount of H_2 adsorbed.

3. Results and discussion

3.1. Characterization of biomass derived ACs

Textural properties of prepared ACs were determined by the adsorption/desorption N_2 isotherms at −196 °C and CO_2 adsorption at 0 °C. All the nitrogen adsorption isotherms depicted in Fig. 1 can be considered as a combination of type I and type IV isotherms, according with the IUPAC categorization [26]. The type I isotherm is characteristic of microporous materials and shows a sharp rise in adsorption at low P/P_o relative pressures and a subsequent plateau parallel to the P/P^0 axis. Type IV isotherms exhibit hysteresis loop associated with capillary condensation in mesopores. The adsorption profiles in Fig. 1 exhibit an initial part similar to type I isotherm, indicating the presence of micropores, but then there is a persistent rise in adsorption as the relative pressure increases and the presence of a hysteresis loop is found. This second part of the isotherm is ascribed to the presence of mesopores. Furthermore, the H4 type sparse hysteresis loop suggests the presence of slit pores [27].

The BET surface area, total pore volume and micropore volume in the range of 1.4–2 nm were determined through nitrogen sorption measurements at −196 °C. Additionally, the diminutive micropore volume (0.3–1.4 nm) was determined utilizing CO_2 adsorption at 0 °C measurements [28]. The textural properties of prepared ACs are

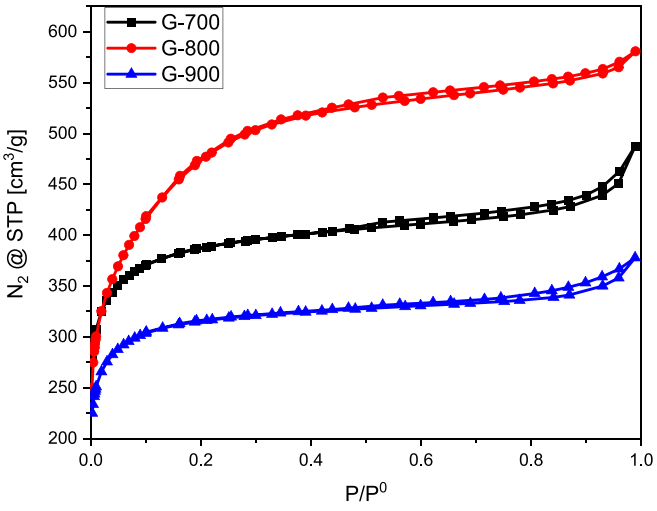

Fig. 1. Nitrogen adsorption–desorption isotherms of ACs produced from common fern.

presented in Table 2. Surface area and total pore volume values within the ranges of 1234–1591 m^2/g and 0.57–0.90 cm^3/g, respectively, were found. The micropore volume of narrow micropores (0.3 to 1.4 nm), reached 0.34–0.62 cm^3/g. Additionally, the micropore volume, as estimated through N_2 adsorption (1.4–2 nm), displayed a range of 0.52 to 0.82 cm^3/g.

The study revealed that a rise in temperature of the carbonization process of the Polypodium vulgare from 700 to 800 °C produces the augmentation of the specific surface area, total pore volume, and micropore volume. Nevertheless, upon reaching 800 °C, a rise in temperature to 900 °C resulted in a partial destruction of the microporous structure as can be seen in Table 3.

Figs. 2 and 3 illustrate the pore size distribution of the ACs, determined from N_2 adsorption at −196 °C and CO_2 adsorption at 0 °C, respectively. Based on the data presented in Fig. 2, it is observed that the ACs examined predominantly comprised micropores, which are characterized by pore sizes of up to 2 nm. Moreover, CO_2 adsorption experiments indicate for all the prepared ACs the existence of pores in the ranges of 0.3–0.4, 0.4–0.5, 0.5–0.7 and 0.8–0.9 nm (Fig. 3). Mesopores with a size of 2–3 nm were also present (Fig. 2). The formation of these pores is attributed to the liberation of non-carbon constituents, such as nitrogen and oxygen, during the process of carbonization; the use of KOH as activating agent further contributes to the development of these pores [29].

The X-ray diffraction (XRD) patterns offer a profound glimpse into the intricate structural evolution of activated carbons (ACs) derived at varying temperatures, specifically at 700 °C, 800 °C, and 900 °C. The discernible features in the form of broad peaks, reaching maxima at 2θ values around 21°, 43°, and 80° (as illustrated in Fig. 4), provide a nuanced understanding of the carbon materials' crystallographic arrangement. The peak situated at 2θ≈21° is emblematic of the (0 0 2) diffraction line. This particular line signifies the ordered stacking of carbon atoms within the crystalline lattice. In the realm of activated carbons, the presence of this peak implies the existence of certain well-defined graphitic layers or planes. Further scrutinizing the XRD patterns, the peaks at 2θ≈43° and 80° can be attributed to the (1 0 0)/(1 0 1) and (1 1 0)/(1 1 2) lines, respectively. Each of these lines corresponds to distinct crystallographic orientations and arrangements within the carbon lattice. The (1 0 0) and (1 0 1) lines at 2θ≈43° unveil specific orientations of graphitic planes, while the (1 1 0) and (1 1 2) lines at 2θ≈80° provide insights into additional crystallographic planes. What adds a layer of complexity to this structural narrative is the observed broadness of these diffraction peaks. This broadening phenomenon is a hallmark feature of a poorly ordered graphite-based structure within carbon materials [30–32]. It suggests a lack of long-range structural order, hinting at the emergence of disordered or amorphous carbon domains. Such disorder is often a consequence of the activation process, where precursor materials undergo transformative changes, resulting in the development of a porous and less organized carbon structure. This poorly ordered graphite-based structure is not a mere happenstance, but a deliberate outcome associated with the thermal treatments at relatively high temperatures during the activation process. This structural disposition plays a pivotal role in defining the unique properties of activated carbons, such as an elevated surface area and heightened adsorption capabilities.

Table 3
Textural parameters of the ACs derived from common fern.

AC sample	BET surface area m^2/g	Total pore volume cm^3/g	Micropore volume (1.4–2 nm)[a] cm^3/g	Micropore volume (0.3–1.4 nm)[b] cm^3/g
G-700	1426	0.60	0.55	0.41
G-800	1591	0.90	0.82	0.62
G-900	1234	0.57	0.52	0.34

[a] determined from N_2 adsorption;
[b] determined from CO_2 adsorption

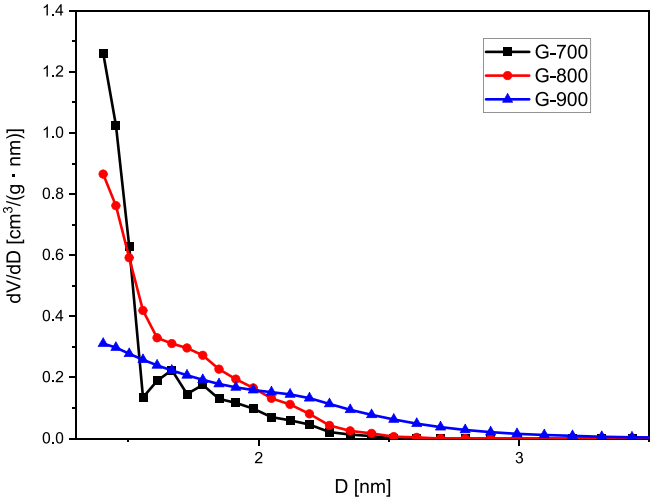

Fig. 2. Pore size distribution of ACs calculated from N_2 adsorption.

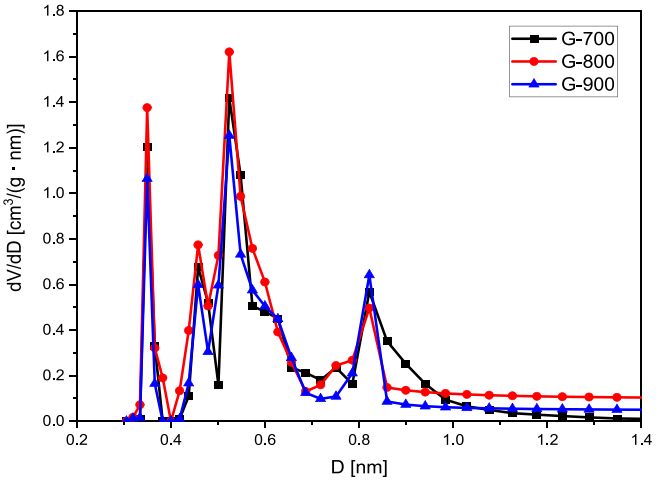

Fig. 3. Micropore size distribution of ACs calculated from CO_2 adsorption.

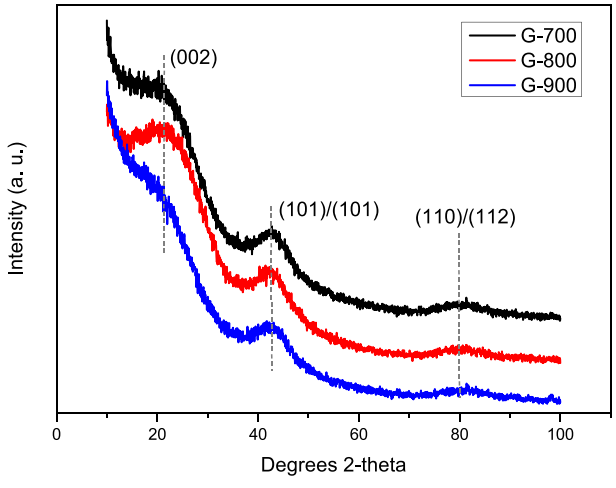

Fig. 4. XRD analysis of ACs prepared at different temperatures.

The FT-IR spectra of the prepared ACs are shown in Fig. 5. All the samples present similar spectral features, where the more characteristic vibrations are observed around 3300–3600, 2760, 2431–2390, 1631,

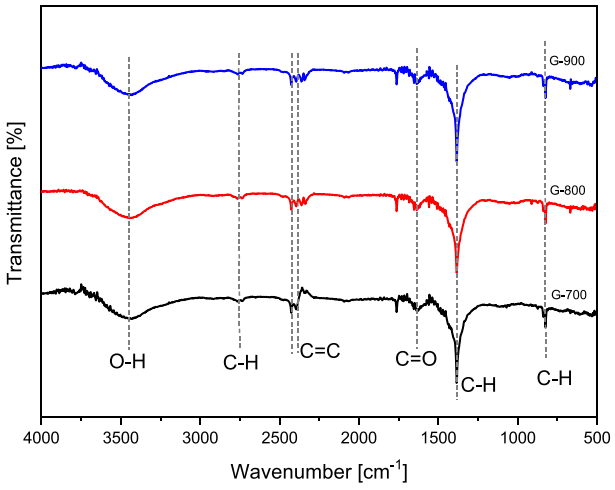

Fig. 5. FT-IR spectra of ACs prepared at different temperatures.

1387, and 828 cm^{-1}. The broad band between 3300 and 3600 cm^{-1} corresponds to the υ(O–H) [32,33]. The band at 2760 cm^{-1} corresponds to the υ (C–H) of the CH_x groups, while the peaks appearing at 2431–2390 cm^{-1} can be attributed to the presence of C═C bonds [34,36]. The peak at 1631 cm^{-1} can be related to the υ(C═O) of carboxylic acids and the peak at 1387 cm^{-1} to the asymmetric and symmetric bending in-plane of the C-H bonds [35,36]. Finally, the band found at 828 cm^{-1} is related to stretching vibrations outside the plane of C – H bonds [36,37]. Functional groups identified by FTIR, such as oxygen-containing moieties (hydroxyl, carbonyl), can influence hydrogen adsorption. Certain functional groups may act as active sites for hydrogen chemisorption, enhancing storage capacity.

Fig. 6 shows the Raman spectra of the ACs prepared at different temperatures. The Raman spectra can reveal the presence of graphitic domains. Higher graphitization is often associated with improved hydrogen storage performance due to enhanced structural stability and increased surface area. In all cases, D and G bands, appearing at about 1300 cm^{-1} (D band) and 1593 cm^{-1} (G band), typical of carbonaceous materials, are present; the D band is associated with disordered carbon materials, while the G band corresponds to the in-plane sp^2 (C = C) vibrations of well-structured graphitic materials. The degree of graphitization can be evaluated using the ratio of intensities of the D and G peaks [37–39]. As observed in Fig. 6, I_D/I_G values were in the 1.2–1.6

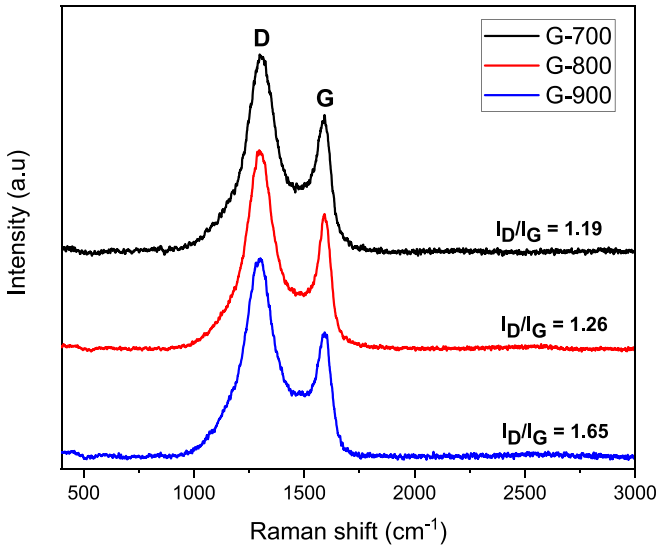

Fig. 6. Raman spectra of ACs prepared at different temperatures.

range. This indicates the presence of a large number of defects and poorly ordered carbon [40–42], according with the XRD results exposed above. Moreover, the I_D/I_G ratio increases with the increase of the carbonization temperature used in the ACs preparation. The decrease in the degree of graphitization of the material can be attributed to a greater alteration of the graphitic domains with the increase of the activation temperature.

Fig. 7 shows SEM and TEM images of ACs prepared. Different shapes, wall thicknesses and the presence of hollows and tunnels can be seen in the images at the microscale. The carbonization step of the materials produces a certain number of pores and voids during the activation due to the gasification process, which determines the final morphology of samples [43–45]. In this case, an increase of the activation temperature from 700 to 900 °C developed a higher fragmentation of the structures. Furthermore, TEM micrograph illustrates an examination of intricate arrangement, demonstrating how the defective graphene-like layers, varying in size and shape, are tightly bound together to form spaces between the graphene layers (microporosity).

3.2. H_2 adsorption performance of biomass-derived ACs

The H_2 adsorption capacity of each AC was investigated to assess the H_2 capture performance. The amount of H_2 adsorbed at equilibrium up to 45 bars was determined at 25, 40, 60, 80 and 100 °C. The H_2 experimental isotherms are depicted in Fig. 8. As expected, the H_2 adsorption capacity increases with rising pressure, at higher pressure, H_2 molecules have more kinetic energy and are more likely to collide with the surface of the adsorbent, resulting in greater adsorption capacity [46]. All isotherms follow a similar trend, the amount of adsorbed H_2 highly increase at low pressures and then the increase slow down as the pressure rises (Fig. 8). On the other hand, an increase in temperature causes a decrease in the adsorption capacity, suggesting an exothermic physical adsorption [47].

Among the three tested samples, G-800 demonstrated the highest H_2 uptake reaching 13.63 mmol/g at 25 °C, under a pressure of 45 bars. At 40 °C, 60 °C, 80 °C, and 100 °C, the H_2 adsorbed amounts for G-800 were 9.61, 6.51, 5.93, and 4.52 mmol/g, respectively. In the case of G-700 and G-900, adsorption capacity values were found to be 10.09 and 8.23 mmol/g at 25 °C. For temperatures varying between 40 and 100 °C, G-700, and G-900 H_2 uptake was in the range of 8.63–3.54 mmol/g and 6.40–2.91 mmol/g, respectively.

The main mechanism of physical adsorption of hydrogen on activated carbon is primarily governed by Van der Waals forces, with a particular emphasis on London dispersion forces (Fig. 9). This physical interaction is often referred to as physisorption, and it plays a crucial role in facilitating the attachment of hydrogen molecules to the surface of activated carbon [48]. Van der Waals forces are attractive forces that arise due to temporary fluctuations in electron distribution within molecules. In the context of hydrogen adsorption on activated carbon, London dispersion forces become especially pertinent. Activated carbon, characterized by a porous structure with a vast surface area, provides an ideal platform for the adsorption of hydrogen. During physisorption, hydrogen molecules approach the activated carbon surface, and the temporary imbalances in electron distribution in both the hydrogen and carbon atoms induce a momentary dipole. This induces a corresponding dipole in neighboring atoms, leading to a chain reaction of induced dipoles [49]. The porous nature of activated carbon, with its network of micropores and mesopores, amplifies the available surface area for physisorption. The extensive surface area, combined with the intrinsic affinity of hydrogen for carbon surfaces, facilitates the accumulation of hydrogen molecules on the activated carbon. It's crucial to note that physisorption is a reversible process, and the adsorption strength is influenced by factors such as temperature and pressure. Lower temperatures and higher pressures generally enhance the physisorption of hydrogen on activated carbon, offering insights into the conditions that optimize this physical interaction [50].

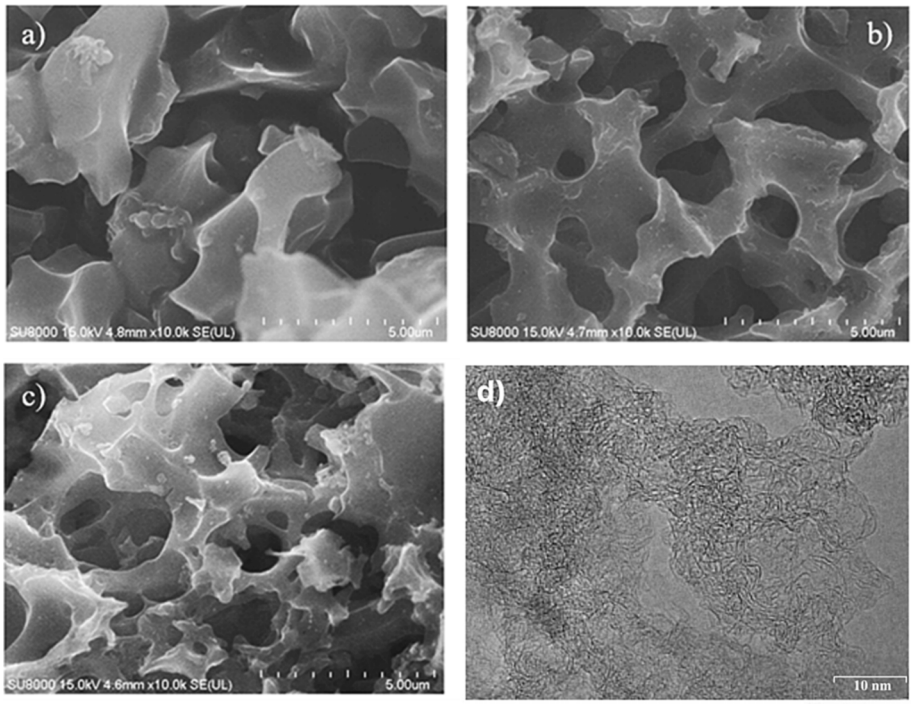

Fig. 7. SEM images of ACs prepared at different temperatures: a) G-700; b) G-800c) G-900 and TEM image of (d) G-800.

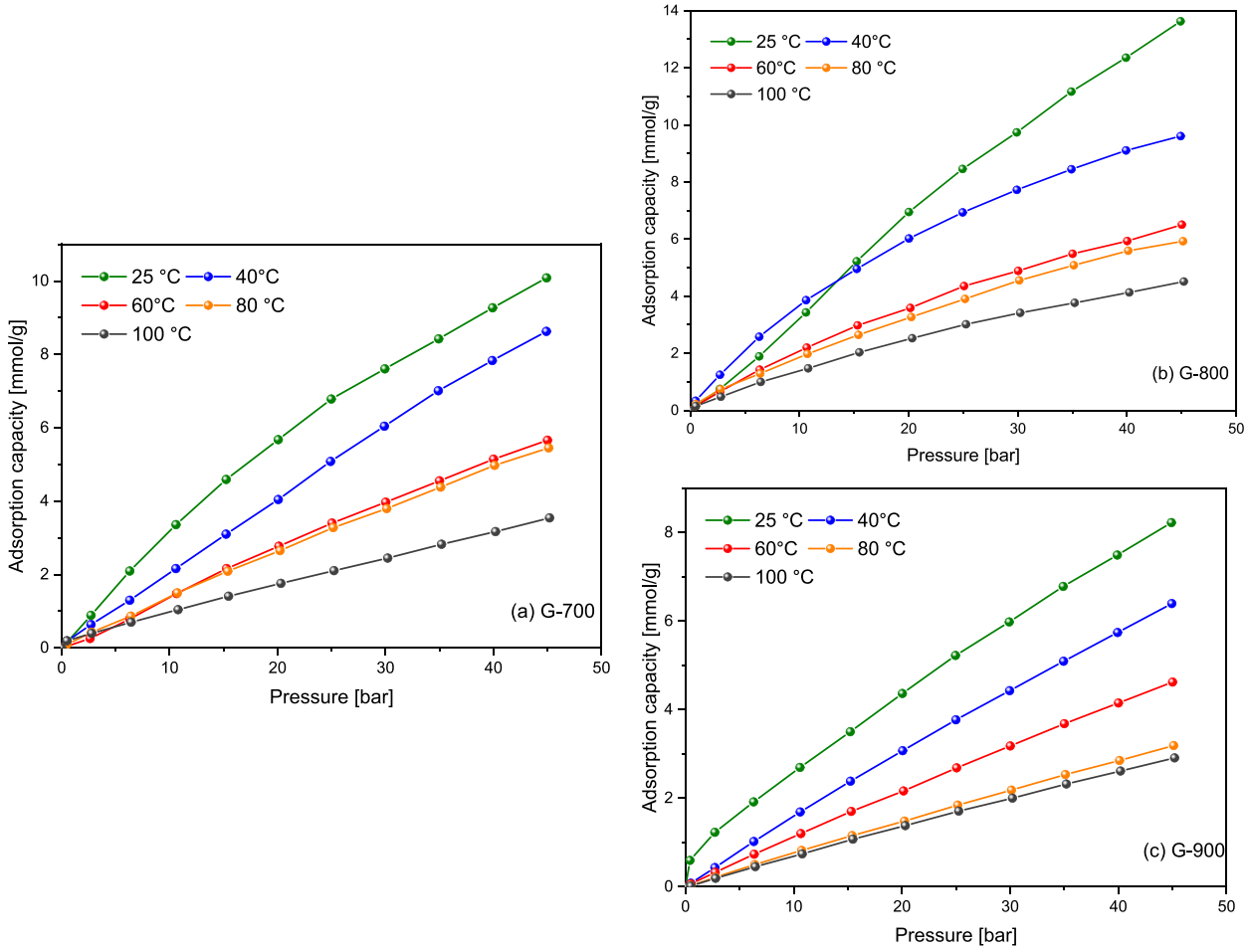

Fig. 8. H_2 adsorption isotherms at different temperatures of a) G-700, b) G-800, and c) G-900.

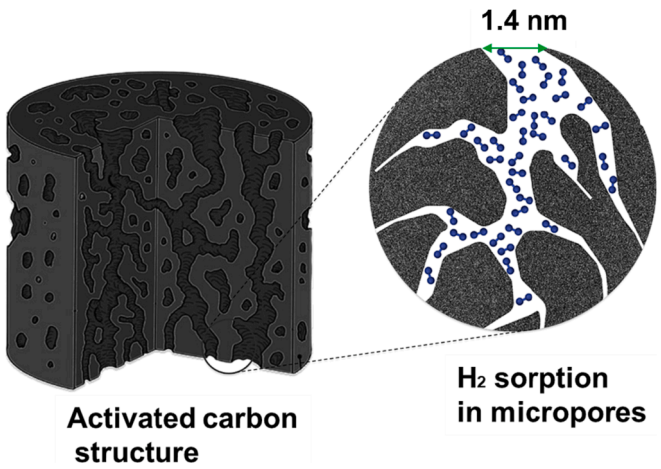

Fig. 9. Schematic illustration of the hydrogen adsorption in the activated carbon microporous structure.

In summary, the main mechanism of physical adsorption of hydrogen on activated carbon involves Van der Waals forces, particularly London dispersion forces. This physisorption mechanism is fundamental to the porous nature of activated carbon and is central to applications such as hydrogen storage.

The higher effectiveness of G-800 adsorbing H_2 compared to G-700 and G-900 should be related with its unique surface, textural and structural properties, following the impact of textural parameters on the sorption of H_2 onto the synthesized ACs. Fig. 9 depicts the relationship between the amount of adsorbed H_2 and textural parameters, including the specific surface (Fig. 10a), total pore volume (Fig. 10b), volume of micropores determined by N_2 adsorption (Fig. 10c) and volume of micropores determined by CO_2 adsorption (Fig. 10d).

The outcomes obtained yielded exceptional findings. It can be noticed that there is a lack of relationship between the H_2 uptake and the total pore volume or micropore volume determined through N_2 sorption (pores in the < 2 nm range). On the other hand, a linear correlation was observed between the H_2 adsorption capacity and the surface area or volume of micropore with pore width below 1.4 nm, This confirms that the N_2 isotherm lacks the capability to assess the size of porosity, especially small sizes (<1.4 nm). As can be seen in Fig. 10, the best linear fitting was obtained between the H_2 adsorption capacity, and the pore volume determined by CO_2 adsorption (R^2 = 0.909–0.999 for all investigated temperatures). The observation indicates that for the ACs prepared in this work, the H_2 capture is most strongly influenced by the presence of small micropores (0.3–1.4 nm) and specific surface area.

3.3. *Modelling of H_2 adsorption processes*

Modeling analysis has been performed to identify the specific factors that contribute to the H_2 adsorption on developed ACs. Experimental adsorption curves for G-800, G-700 and G-900 shown in Fig. 8a-c, were modelled according to Langmuir, Freundlich, Temkin, Redlich–Peterson, Toth, Hill, Koble–Corrigan, Sips, and Radke–Prausnitz models (Table 1). As an example, for the most performant AC in H_2 adsorption, G-800, the fittings of adsorption experimental curves are plotted in Fig. 10. Table S1 provides a summary of the estimated SSE values for each isotherm model based on non-linear regression; the corresponding isotherms' parameters are given in Table S2.

As can be seen in Fig. 10 and Table S1, the Temkin model is not appropriate for the description of H_2 adsorption onto the ACs developed in this work; the underlying assumption of this model is that the solid surface is homogenous. Among the eight remaining isotherm models, except for G-900 at 25 °C, Hill, Koble-Corrigan and Sips equations can provide a good description of H_2 adsorption capacities of ACs in the range 25–100 °C (SSE: 0.0006–0.0622). The Hill, Koble-Corrigan, and

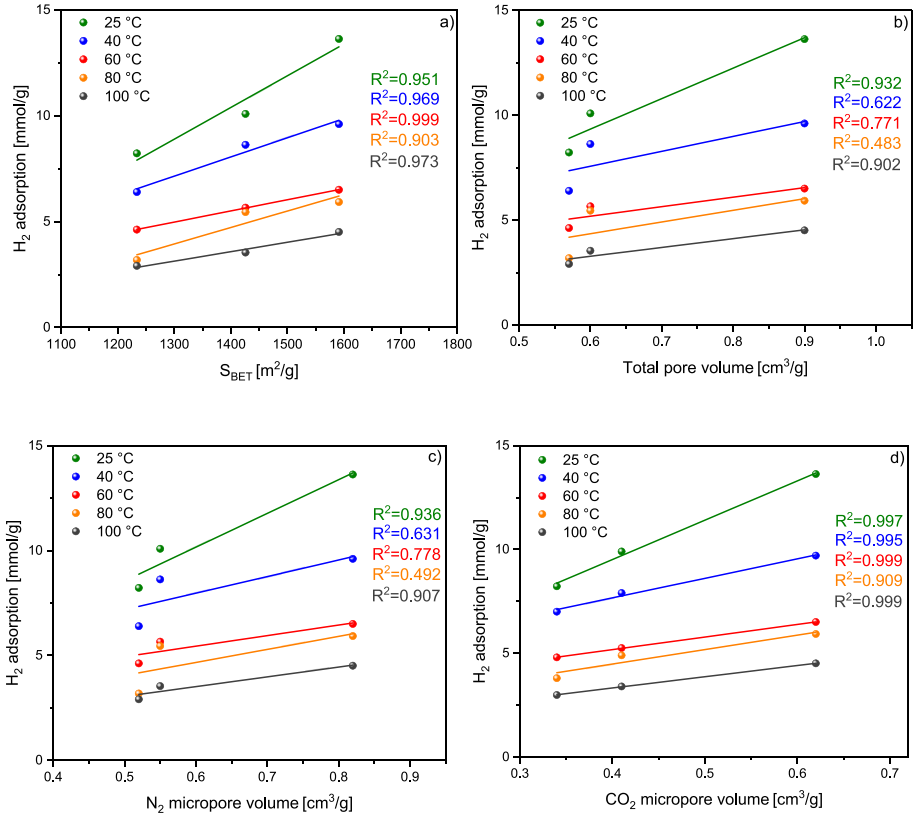

Fig. 10. Relationship between different textural parameters and the amount of H_2 adsorbed at 25 °C, 40 °C, 60 °C, 80 °C and 100 °C and 45 bar.

Sips models are three distinct approaches used to characterize the adsorption capacities of hydrogen on activated carbons. The Hill model is specifically designed for cooperative adsorption, capturing situations where the binding of one hydrogen molecule enhances the adsorption of others. The Koble-Corrigan model, an extension of the Langmuir equation, is capable of accommodating deviations from ideal behavior, making it versatile for systems involving both monolayer and multilayer adsorption. Meanwhile, the Sips model, which combines elements of the Langmuir and Freundlich models, excels at describing heterogeneous adsorption processes, particularly when both monolayer and multilayer adsorption occur simultaneously. While the Hill model emphasizes cooperativity, the Koble-Corrigan and Sips models offer flexibility to cater to a wide range of adsorption behaviors. Based on the best fitted isotherm equation (Sips), surfaces may exhibit heterogeneity due to changes in surface energy, active sites, and surface roughness. These variances have the potential to result in deviations from the linear behavior that is expectedby the Temkin model.

One of the important criteria for assessing the quality of a good activated carbon as an adsorbent is its regenerative capacity. It determines the lifetime of the adsorbent, its reuse, and the total cost of capture. To assess the possibility of an easy regeneration and reuse of the material, for the best sorbent, G-800, the reversibility of H_2 adsorption was tested in 1, 3, 5, and 10 cycles at 25 °C (Fig. 11), 40 °C (Fig. S1a), 60 °C (Fig. S1b), 80 °C (Fig. S1c), and 100 °C (Fig. S1d) up to 45 bar. Based on this measurement, it is possible to assess the regeneration capacity of activated carbons, and secondly, to verify the fact that H_2 does not bind to the sorbent material by chemisorption. In addition, it allows to establish parameters that can serve as a reference point when trying to regenerate in real conditions on an industrial scale. As can be seen in Fig. 12 and Figure S1a-d, after many cycles of H_2 adsorption, no changes were found. The highest standard deviation for H_2 uptake in the different cycles was 5 %. The results confirm that the G-800 AC prepared in this work, can be easily regenerated under mild conditions and that it retained its properties. Activated carbon G-800 meets the criterion of a good sorbent in terms of its ability of regeneration.

3.4. Isosteric heat of H_2 adsorption

The isosteric heat of H_2 adsorption (Q_{st}) was estimated from the H_2 isotherm experimental data for all AC samples, at 25, 40, 60, 80 and 100 °C, using the Clausius–Clapeyron equation (Eq. (2)). Based on the isotherm model widely reported in the literature, which was Sips model, the pressure values for each temperature for the same degree of surface covering were then determined directly from the isotherm equation translation into function $p = f(\theta)$ by non-linear regression. After establishing the partial pressure values for a particular surface coverage on AC in the range of 0.005–0.35 at five temperatures, the adsorption isosteres were plotted (ln(p) versus the 1/T). The Qst values as a function of the H_2 coverage were obtained from the slope ($-Q_{st}/R$). The isosteric heat of H_2 adsorption on ACs decreased considerably as coverage increased (Fig. 12). As expected, the greater the degree of surface covering, the weaker the interaction between H_2 and ACs. For a given coverage, the Q_{st} values were in the order G-800 > G-700 > G-900, according with the amount of narrow pores, especially ultramicropores,

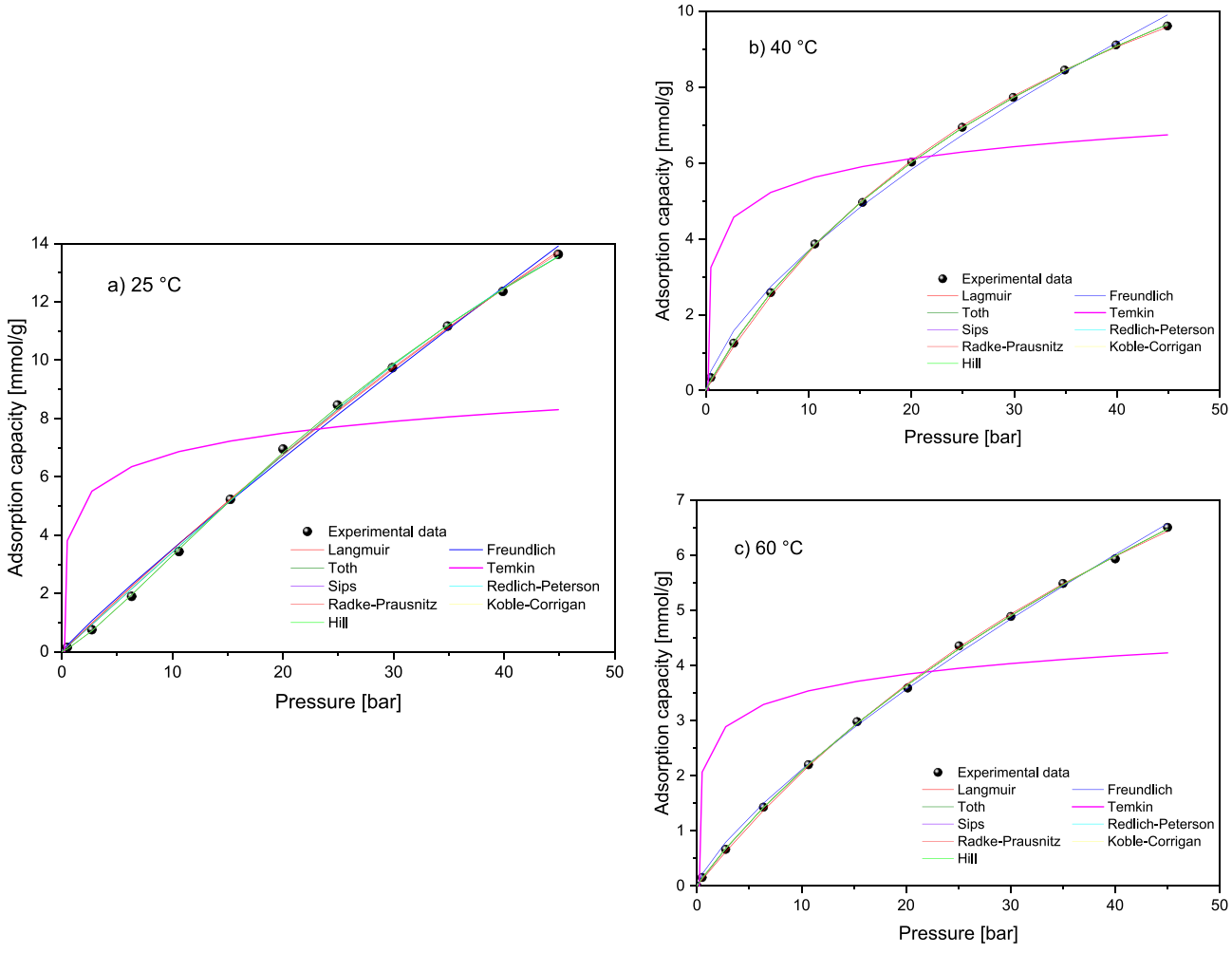

Fig. 11. Fitting of H_2 adsorption isotherms to selected models for G-800 at a) 25 °C, b) 40 °C, c) 60 °C, d) 80 °C and e) 100 °C.

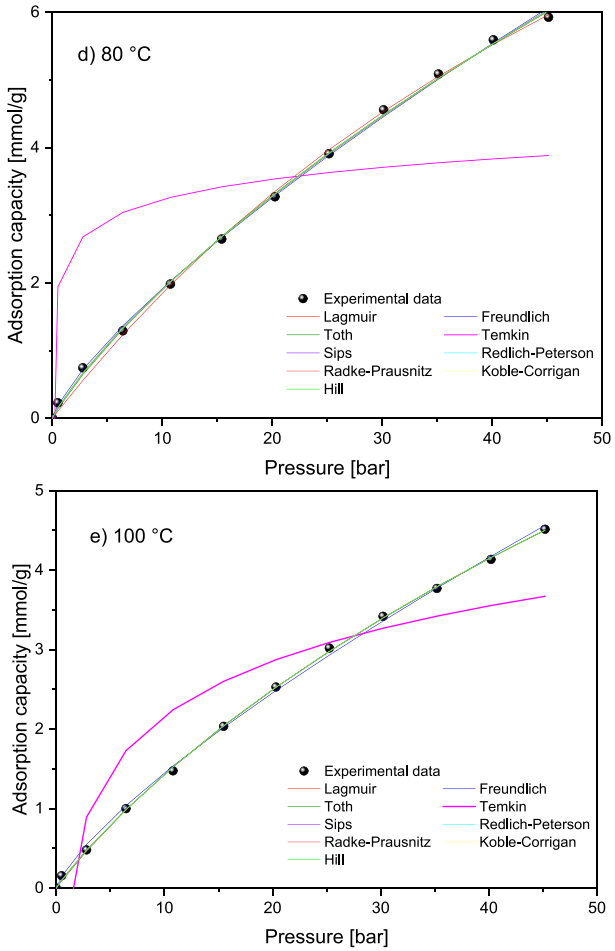

Fig. 11. (*continued*).

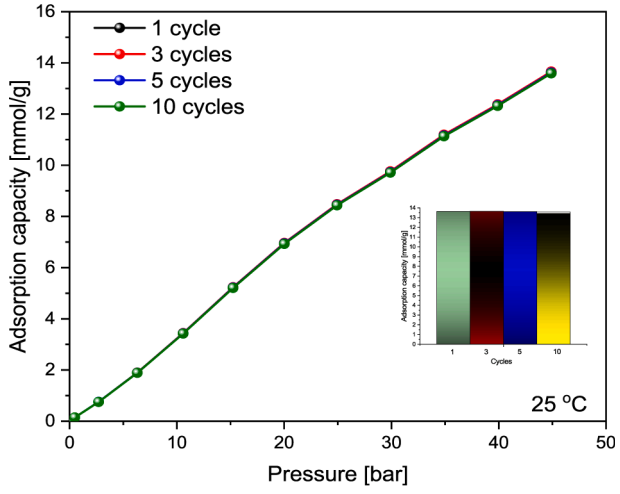

Fig. 12. Multi-cycle H_2 adsorption isotherms for G-800 at 25 °C in 1st, 3rd, 5th and 10th cycles.

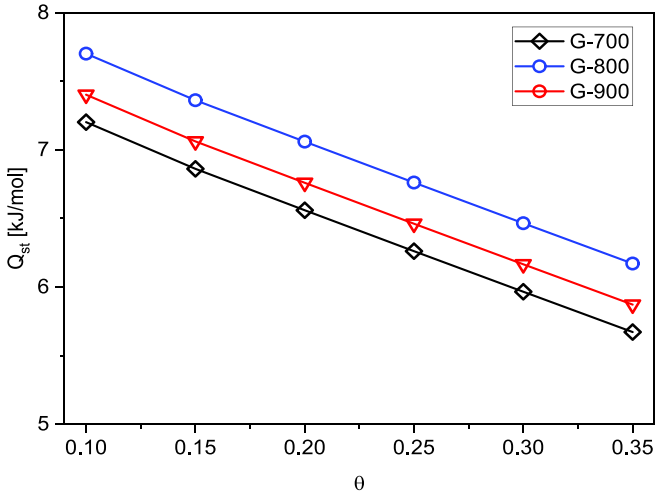

Fig. 13. Change of the isosteric heat of H_2 adsorption as a function of surface coverage for the different ACs.

due to the overlapping of Van der Waals forces present [51] (Fig. 13). The calculated Qst values ranged from 7.7 to 5.7 kJ/mol (Fig. 12), which is consistent with other reported studies in the literature [51,52].

The values of isosteric heat suggest that the adsorption of hydrogen on activated carbons is achieved by physisorption. This phenomenon occurs without any chemical bonds between H_2 and the ACs surface at a given pressure and temperature and especially depends on the textural properties of the AC. It is widely known that hydrogen interacts with the carbon surface through van der Waals interactions [53–55]. For activated carbon, hydrogen can be rapidly adsorbed into small micropores that lie within larger micropores and/or mesopores. The kinetic diameter of the H_2 molecules (~0.289 nm) fits well with the pore diameters determined by CO_2 adsorption (0.3–1.4 nm); heterogeneous pore sizes lead to a non-uniform adsorption rate. Physical adsorption is

thermodynamically favored at low temperatures and high pressures, which allows high H_2 adsorption and storage efficiency. Activated carbons have, on average, the highest hydrogen adsorption capacities among currently known nanotextured carbon materials, where in addition exhibits rapid adsorption/desorption kinetics [52,56].

4. Conclusions

Activated carbons derived from common fern biomass emerges as a promising solution for effective and sustainable medium-pressure hydrogen storage. The materials, prepared through KOH activation and carbonization at temperatures ranging from 700 to 900 °C, exhibit exceptional properties that distinguish them in the field:

- ACs possess a highly microporous structure and high values of BET surface area, up to 1591 m^2/g. A
- Noteworthy porosity is observed, with the total pore volume ranging from 0.57 to 0.90 cm3/g, and the micropore volume ranging from 0.52 to 0.82 cm3/g.
- The AC, which was prepared at 800 °C, exhibited the highest H_2 adsorption capacity. Specifically, at 45 bar, the H_2 uptake was 13.63 (2.73 wt%), 9.61 (1.92 wt%), 6.51 (1.302 wt%), 5.93 (1.186 wt%), and 4.52 (0.904 wt%) mmol/g at temperatures of 25, 40, 60, 80 and 100 °C, respectively. The superior H_2 adsorption performance was mainly attributed to the amount of micropores with width below 1.4 nm and the specific surface area.
- The reusability of the most performant AC sample was demonstrated during at least 10 adsorption/desorption cycles.
- The isosteric heats of H_2 adsorption were within the range of 5.7–7.7 kJ/mol for coverage between 0.10 and 0.35, clearly suggesting a physisorption phenomenon.
- Among them the Sips model, that suggests an heterogenous adsorption system.

In conclusion, the utilization of ACs derived from Polypodium vulgare, a commonly available feedstock, for effective medium-pressure H_2 storage not only provides a sustainable and accessible solution but also holds the potential to significantly contribute to our efforts in developing clean and efficient energy storage technologies for a more sustainable future.

CRediT authorship contribution statement

Jarosław Serafin: Conceptualization, Methodology, Validation, Formal analysis, Investigation, Data curation, Writing – original draft, Writing – review & editing, Project administration, Supervision. **Bartosz Dziejarski:** Conceptualization, Methodology, Software, Formal analysis, Investigation, Data curation, Writing – original draft, Writing – review & editing. **Carlos Solis:** Data curation, Writing – original draft. **Pilar Ramírez de la Piscina:** Formal analysis, Writing – original draft. **Narcis Homs:** Formal analysis, Writing – original draft.

Declaration of competing interest

The authors declare that they have no known competing financial interests or personal relationships that could have appeared to influence the work reported in this paper.

Data availability

Data will be made available on request.

Acknowledgments

The authors are thankful to MICINN PID2020-116031RB I00/AEI/10.13039/501100011033/FEDER project for financial support. Jarosław Serafin acknowledge financial support from Grant TED2021-132070B-C21 funded by the Spanish Ministry for Science and Innovation.

Appendix A. Supplementary data

Supplementary data to this article can be found online at https://doi.org/10.1016/j.fuel.2024.130975.

References

[1] Li X, Sun X, Song Q, Yang Z, Wang H, Duan Y. A critical review on integrated system design of solar thermochemical water-splitting cycle for hydrogen production. Int J Hydrogen Energy 2022;47(79):33619–42.
[2] Serafin J, Dziejarski B. Activated carbons—preparation, characterization and their application in CO2 capture: A review. Environ Sci Pollut Res 2023:1–55.
[3] Dziejarski B, Serafin J, Andersson K, Krzyżyńska R. CO2 capture materials: a review of current trends and future challenges. Materials Today Sustainability 2023;24:100483.
[4] Dawood F, Anda M, Shafiullah GM. Hydrogen production for energy: An overview. Int J Hydrogen Energy 2020;45(7):3847–69.
[5] Sazali N. Emerging technologies by hydrogen: a review. Int J Hydrogen Energy 2020;45(38):18753–71.
[6] Widera B. Renewable hydrogen implementations for combined energy storage, transportation and stationary applications. Therm Sci Eng Progress 2020;16:100460.
[7] Abe JO, Popoola API, Ajenifuja E, Popoola OM. Hydrogen energy, economy and storage: review and recommendation. Int J Hydrogen Energy 2019;44(29):15072–86.
[8] Tashie-Lewis BC, Nnabuife SG. Hydrogen production, distribution, storage and power conversion in a hydrogen economy-a technology review. Chem Eng J Adv 2021;8:100172.
[9] Eberle U, Felderhoff M, Schueth F. Chemical and physical solutions for hydrogen storage. Angew Chem Int Ed 2009;48(36):6608–30.
[10] Tarasov BP, Lototskii MV, Yartys VA. Problem of hydrogen storage and prospective uses of hydrides for hydrogen accumulation. Russ J Gen Chem 2007;77(4):694–711.
[11] Rusman NAA, Dahari M. A review on the current progress of metal hydrides material for solid-state hydrogen storage applications. Int J Hydrogen Energy 2016;41(28):12108–26.
[12] Mashhadimoslem H, Safarzadeh Khosrowshahi M, Delpisheh M, Convery C, Rezakazemi M, Aminabhavi TM, et al. Green ammonia to hydrogen: reduction and oxidation catalytic processes. Chem Eng J 2023;474:145661.
[13] Mashhadimoslem H, Ghaemi A, Maleki A, Elkamel A. Enhancement of oxygen adsorption using biomass-based oxidized porous carbon. J Environ Chem Eng 2023;11(2):109300.
[14] Thanh HV, Ebrahimnia Taremsari S, Ranjbar B, Mashhadimoslem H, Rahimi E, Rahimi M, et al. Hydrogen storage on porous carbon adsorbents: rediscovery by nature-derived algorithms in random forest machine learning model. Energies 2023;16(5):2348.
[15] Czarna-Juszkiewicz D, Cader J, Wdowin M. From coal ashes to solid sorbents for hydrogen storage. J Clean Prod 2020;270:122355.
[16] Nazir G, Rehman A, Hussain S, Aftab S, Heo K, Ikram M, et al. Recent advances and reliable assessment of solid-state materials for hydrogen storage: a step forward toward a sustainable H2 economy. Adv Sustain Syst 2022;6(11):2200276.
[17] Rimza T, Saha S, Dhand C, Dwivedi N, Patel SS, Singh S, et al. Carbon-based sorbents for hydrogen storage: challenges and sustainability at operating conditions for renewable energy. ChemSusChem 2022;15(11).
[18] Li Y, Yang RT. Hydrogen storage in low silica type X zeolites. J Phys Chem B 2006;110(34):17175–81.
[19] Murray LJ, Dincă M, Long JR. Hydrogen storage in metal–organic frameworks. Chem Soc Rev 2009;38(5):1294–314.
[20] Mohan M, Sharma VK, Kumar EA, Gayathri V. Hydrogen storage in carbon materials—A review. Energy Storage 2019;1(2):e35.
[21] Yorgun S, Yıldız D. Preparation and characterization of activated carbons from Paulownia wood by chemical activation with H3PO4. J Taiwan Inst Chem Eng 2015;53:122–31.
[22] Ng JCY, Cheung WH, McKay G. Equilibrium studies of the sorption of Cu (II) ions onto chitosan. J Colloid Interface Sci 2002;255(1):64–74.
[23] Sircar S, Mohr R, Ristic C, Rao MB. Isosteric heat of adsorption: theory and experiment. J Phys Chem B 1999;103(31):6539–46.
[24] Karaman C, Karaman O, Show P-L, Karimi-Maleh H, Zare N. Congo red dye removal from aqueous environment by cationic surfactant modified-biomass derived carbon: equilibrium, kinetic, and thermodynamic modeling, and forecasting via artificial neural network approach. Chemosphere 2022;290:133346.
[25] Thommes M, Kaneko K, Neimark AV, Olivier JP, Rodriguez-Reinoso F, Rouquerol J, et al. Physisorption of gases, with special reference to the evaluation of surface area and pore size distribution (IUPAC Technical Report). Pure Appl Chem 2015;87(9–10):1051–69.
[26] Serafin J, Dziejarski B. Application of isotherms models and error functions in activated carbon CO2 sorption processes. Microporous Mesoporous Mater 2023;354:112513.

[27] Wu Z, He S, Han Y, Zhai G, He X, Zhou Z. Effect of organic matter type and maturity on organic matter pore formation of transitional facies shales: a case study on upper Permian Longtan and Dalong shales in middle Yangtze region, China. J Earth Sci 2020;31(2):368–84.
[28] Sreńscek-Nazzal J, Kiełbasa K. Advances in modification of commercial activated carbon for enhancement of CO2 capture. Appl Surf Sci 2019;494:137–51.
[29] Serafin J, Narkiewicz U, Morawski AW, Wróbel RJ, Michalkiewicz B. Highly microporous activated carbons from biomass for CO2 capture and effective micropores at different conditions. J CO2 Util 2017;18:73–9.
[30] Sonal S, Prakash P, Mishra BK, Nayak GC. Synthesis, characterization and sorption studies of a zirconium(IV) impregnated highly functionalized mesoporous activated carbons. RSC Adv 2020;10(23):13783–98.
[31] Li ZQ, Lu CJ, Xia ZP, Zhou Y, Luo Z. X-ray diffraction patterns of graphite and turbostratic carbon. Carbon 2007;45(8):1686–95.
[32] Mojoudi N, Mirghaffari N, Soleimani M, Shariatmadari H, Belver C, Bedia J. Phenol adsorption on high microporous activated carbons prepared from oily sludge: Equilibrium, kinetic and thermodynamic studies. Sci Rep 2019;9(1):19352.
[33] Serafin J, Dziejarski B, Cruz Junior OF, Sreńscek-Nazzal J. Design of highly microporous activated carbons based on walnut shell biomass for H2 and CO2 storage. Carbon 2023;201:633–47.
[34] Olivares-Marín M, Fernández-González C, Macías-García A, Gómez-Serrano V. Preparation of activated carbons from cherry stones by activation with potassium hydroxide. Appl Surf Sci 2006;252(17):5980–3.
[35] Kaur J, Sharma JP, Singh N, Pathak D, Guleria N, Singh PK, et al. Improvement in optical absorption and emission characteristics of polymethyl methacrylate in solution cast polymethyl methacrylate/polyvinyl carbazole polyblends. J Thermoplast Compos Mater 2023;36(8):3260–9.
[36] Shi G, Liu C, Wang G, Chen X, Li L, Jiang X, et al. Preparation and electrochemical performance of electrospun biomass-based activated carbon nanofibers. Ionics 2019;25(4):1805–12.
[37] Gupta GK, Sagar P, Pandey SK, Srivastava M, Singh AK, Singh J, et al. In situ fabrication of activated carbon from a bio-waste desmostachya bipinnata for the improved supercapacitor performance. Nanoscale Res Lett 2021;16(1):85.
[38] Keppetipola NM, Dissanayake M, Dissanayake P, Karunarathne B, Dourges MA, Talaga D, et al. Graphite-type activated carbon from coconut shell: a natural source for eco-friendly non-volatile storage devices. RSC Adv 2021;11(5):2854–65.
[39] Liu Y, Liu X, Dong W, Zhang L, Kong Q, Wang W. Efficient adsorption of sulfamethazine onto modified activated carbon: a plausible adsorption mechanism. Sci Rep 2017;7(1):12437.
[40] Katz S, Pevzner A, Shepelev V, Marx S, Rotter H, Amitay-Rosen T, et al. Activated carbon aging processes characterization by Raman spectroscopy. MRS Adv 2022;7 (12):245–8.
[41] To JWF, Chen Z, Yao H, He J, Kim K, Chou H-H, et al. Ultrahigh surface area three-dimensional porous graphitic carbon from conjugated polymeric molecular framework. ACS Cent Sci 2015;1(2):68–76.
[42] Tazibet S, Velasco LF, Lodewyckx P, Abou M'Hamed D, Boucheffa Y. Study of the carbonization temperature for a chemically activated carbon: Influence on the textural and structural characteristics and surface functionalities. J Porous Mater 2018;25(2):329–40.
[43] Guo Y, Wang Q. Fabrication and characterization of activated carbon from Phyllostachys edulis using single-step KOH activation with different temperatures. Processes 2022;10(9):1712.
[44] Wang F. Novel high performance magnetic activated carbon for phenol removal: equilibrium, kinetics and thermodynamics. J Porous Mater 2017;24(5):1309–17.
[45] Thithai V, Jin X, Ajaz Ahmed M, Choi J-W. Physicochemical Properties of activated carbons produced from coffee waste and empty fruit bunch by chemical activation method. Energies 2021;14(11):3002.
[46] Jalil AA, Triwahyono S, Yaakob MR, Azmi ZZA, Sapawe N, Kamarudin NHN, et al. Utilization of bivalve shell-treated Zea mays L. (maize) husk leaf as a low-cost biosorbent for enhanced adsorption of malachite green. Bioresour Technol 2012; 120:218–24.
[47] Wilson SMW, Al-Enzi F, Gabriel VA, Tezel FH. Effect of pore size and heterogeneous surface on the adsorption of CO2, N2, O2, and Ar on carbon aerogel, RF aerogel, and activated carbons. Microporous Mesoporous Mater 2021;322: 111089.
[48] Belhachemi M. Adsorption of organic compounds on activated carbons. In: Sorbents Materials for Controlling Environmental Pollution. Elsevier; 2021. p. 355–85.
[49] Van der Lubbe SC, Fonseca Guerra C. The nature of hydrogen bonds: a delineation of the role of different energy components on hydrogen bond strengths and lengths. Chem –Asian J 2019;14(16):2760–9.
[50] Bosu S, Rajamohan N. Recent advancements in hydrogen storage-Comparative review on methods, operating conditions and challenges. Int J Hydrogen Energy 2023.
[51] Sdanghi G, Schaefer S, Maranzana G, Celzard A, Fierro V. Application of the modified Dubinin-Astakhov equation for a better understanding of high-pressure hydrogen adsorption on activated carbons. Int J Hydrogen Energy 2020;45(48): 25912–26.
[52] Kostoglou N, Koczwara C, Stock S, Tampaxis C, Charalambopoulou G, Steriotis T, et al. Nanoporous polymer-derived activated carbon for hydrogen adsorption and electrochemical energy storage. Chem Eng J 2022;427:131730.
[53] Ramirez-Vidal P, Canevesi RLS, Sdanghi G, Schaefer S, Maranzana G, Celzard A, et al. A Step forward in understanding the hydrogen adsorption and compression on activated carbons. ACS Appl Mater Interfaces 2021;13(10):12562–74.
[54] Fomkin A, Pribylov A, Men'shchikov I, Shkolin A, Aksyutin O, Ishkov A, et al. Adsorption-based hydrogen storage in activated carbons and model carbon structures. Reactions 2021;2(3):209–26.
[55] Sharma G, Sharma S, Kumar A, Lai CW, Naushad Mu, Shehnaz, et al. Activated carbon as superadsorbent and sustainable material for diverse applications. Adsorpt Sci Technol 2022;2022:1–21.
[56] Harjanto S, Fatriansyah JF, Noviana LN, Yunior SW. The Hydrogen adsorption behavior of mechano-chemically activated carbon from Indonesian low-rank coal: coupled Langmuir and Dubinin-Astakhov isotherm model analysis. Int J Technol 2018;9(5):993.
[57] Langmuir I. The adsorption of gases on plane surfaces of glass, mica and platinum. J Am Chem Soc 1918;40(9):1361–403.
[58] Freundlich HMF. Over the adsorption in solution. J Phys Chem 1906;57(385471): 1100–7.
[59] Redlich OJDL, Peterson DL. A useful adsorption isotherm. J Phys Chem 1959;63 (6):1024.
[60] Toth J. State equation of the solid-gas interface layers. Acta Chim Hung 1971;69: 311–28.
[61] Hill AV. The possible effects of the aggregation of the molecules of haemoglobin on its dissociation curves. J Physiol 1910;40:4–7.
[62] Koble RA, Corrigan TE. Adsorption isotherms for pure hydrocarbons. Ind Eng Chem 1952;44(2):383–7.
[63] Sips R. Combined form of Langmuir and Freundlich equations. J Chem Phys 1948; 16(429):490–5.
[64] Radke CJ, Prausnitz JM. Adsorption of organic solutes from dilute aqueous solution of activated carbon. Ind Eng Chem Fundam 1972;11(4):445–51.
[65] Temkin MI. Kinetics of ammonia synthesis on promoted iron catalysts. Acta Physiochim URSS 1940;12:327–56.